# *Electronic Supplementary Information*

# Chalcogen-vacancy group VI transition metal dichalcogenide nanosheets for electrochemical and photoelectrochemical hydrogen evolution

In Hye Kwak,† Ik Seon Kwon,† Jong Hyun Lee, Young Rok Lim, and Jeunghee Park*

*Department of Advanced Materials Chemistry, Korea University, Sejong 339-700, Korea*

*To whom correspondence should be addressed; E-mail: parkjh@korea.ac.kr

I.H.K. and I.S.K. contribute equally as first author.

**Contents**

**Experimental Section**

**Table. S1** Previous works for Si-based PEC cells for hydrogen evolution.

**Fig. S1** SEM, EDX, and XRD data of $MoO_3$ and $WO_3$.

**Fig. S2** XRD data of all samples.

**Fig. S3** HAADF STEM and EDX data of Si-$MoS_2$, Si-$MoSe_2$, Si-$WS_2$, and Si-$WSe_2$.

**Fig. S4** SEM/EDX data and composition of Si-$MoS_2$, Si-$MoSe_2$, Si-$WS_2$, and Si-$WSe_2$.

**Fig. S5** XPS data of Si-$MoS_2$, Si-$MoSe_2$, Si-$WS_2$, and Si-$WSe_2$.

**Fig. S6** SEM images of $MoS_2$, $MoSe_2$, $WS_2$, and $WSe_2$ nanosheets

**Fig. S7** SEM/EDX data and composition of $MoS_2$, $MoSe_2$, $WS_2$, and $WSe_2$ nanosheets

**Fig. S8** ESR data of $MoS_2$, $MoSe_2$, $WS_2$, and $WSe_2$ nanosheets

**Fig. S9** XPS data of $MoS_2$, $MoSe_2$, $WS_2$, and $WSe_2$ nanosheets.

**Fig. S10** XRD, XPS, STEM and EDX of the samples after PEC 3 h test.

**Fig. S11** EIS data of Si-$MoS_2$, Si-$MoSe_2$, Si-$WS_2$, and Si-$WSe_2$.

**Fig. S12** Mott-Schottky plot of Si-$MoS_2$, Si-$MoSe_2$, Si-$WS_2$, and Si-$WSe_2$.

**Fig. S13** EIS data of free-standing $MoS_2$, $MoSe_2$, $WS_2$, and $WSe_2$ nanosheets.

**Fig. S14** Double-layer capacitance of $MoS_2$, $MoSe_2$, $WS_2$, and $WSe_2$ nanosheets.

**References**

**Experimental Section**

(1) Characterization.

The products were characterized by field-emission transmission electron microscopy (FE TEM, FEI TECNAI G2 200 kV, Jeol JEM 2100F, HVEM). Energy-dispersive X-ray fluorescence spectroscopy (EDX) with elemental maps was measured using a TEM (FEI Talos F200X) operated at 200 kV that equipped with high-brightness Schottky field emission electron source (X-FEG) and Super-X EDS detector system (Bruker Super-X). This EDX has powerful sensitivity and resolution in the low photon energy region. Fast Fourier-transform (FFT) images were generated by the inversion of the TEM images using Digital Micrograph GMS1.4 software (Gatan Inc.).

High-resolution X-ray diffraction (XRD) patterns were obtained using the 9B and 3D beamlines of the Pohang Light Source (PLS) with monochromatic radiation ($\lambda$ = 1.54595 Å). XRD pattern measurements were also carried out in a Rigaku D/MAX-2500 V/PC using Cu $K_\alpha$ radiation ($\lambda$ = 1.54056 Å). X-ray photoelectron spectroscopy (XPS) measurements were performed using the 8A1 and 10A2 beam lines of the PLS, as well as a laboratory-based spectrometer (Thermo Scientific Theta Probe) using a photon energy of 1486.6 eV (Al K$\alpha$). Electron spin resonance (ESR) measurements were performed on a Bruker EMX-Plus spectrometer at room temperature. The samples (10 mg) were loaded in a quartz tube. The microwave frequency was 9.644564 GHz, and the microwave power was fixed to 20 mW to avoid saturation.

(2) Water-splitting PEC cell

The backside of NW substrate was connected to a copper (Cu) wire (diameter = 1 mm) using Ga/In eutectic alloy (≥ 99.99%, Sigma-Aldrich) and conductive silver paste (resistivity = < 50

μΩ·cm, Dotite D-500, Fujikura Kasei Co.), and then covered with epoxy glue (Hysol 1C, Loctite). The exposed area of the front side was usually 0.25 $cm^2$. The PEC cells with a three-electrode system was characterized using an electrochemical analyzer (CompactStat, Ivium Technologies). A 450 W Xe lamp (EUROSEP Instruments) was used with an AM1.5G filter, and the light intensity (100 mW $cm^{-2}$) was calibrated using a Si solar cell (Abet Technologies, Model 15150 Reference Cell).

The Si NW electrodes were used as photocathode in 0.5 M $H_2SO_4$ electrolyte (pH 0). A saturated calomel electrode (SCE, saturated KCl, Basi Model RE-2BP) was used as the reference electrode, and a Pt wire (0.5 mm dia., Pine Instrument) was used as the counter electrode. The potentials were referenced to the RHE. +The hydrogen ($H_2$) and oxygen ($O_2$) gas evolution in the PEC cells was monitored using gas chromatography (GC, Young Lin ACME 6100). The electrolyte was purged with helium gas (≥99.999%). A pulsed discharge detector (VICI, Valco Instruments Co., Inc.) and a GC column (SUPELCO Molecular Sieve 13X) were used. The quantities of $H_2$ and $O_2$ were calibrated using standard $H_2$/He and $O_2$/He mixtures, respectively. Faradaic efficiency (FE) for $H_2/O_2$ generation was calculated using the equations: $FE\ (H_2) = \frac{2\ \times N_{H_2} \times 96485}{Q}$ and : $FE\ (O_2) = \frac{4\ \times\ N_{O_2} \times 96485}{Q}$ where $N_{H2}$ or $N_{O2}$ is the amounts (in mol) of $H_2$ or $O_2$, and $Q$ is the generated charge (= photocurrent × time) in Coulomb.

(3) Electrochemical Measurements

Experiments were carried in a three-electrode cell connected to an electrochemical analyzer (CompactStat, Ivium Technologies). HER electrocatalysis (in 0.5 M $H_2SO_4$ electrolyte) was measured using a linear sweeping from 0 to -0.6 V (*vs*. RHE) with a scan rate of 2 mV $s^{-1}$. A saturated calomel electrode (SCE, KCl saturated, Pine Instrument) was used as a reference electrode, and a graphite rod (6 mm dia. × 102 mm long, 99.9995%, Pine Instrument) was used as a counter electrode. The electrolyte was purged with $H_2$ (ultrahigh grade purity 99.999%) during the measurement.

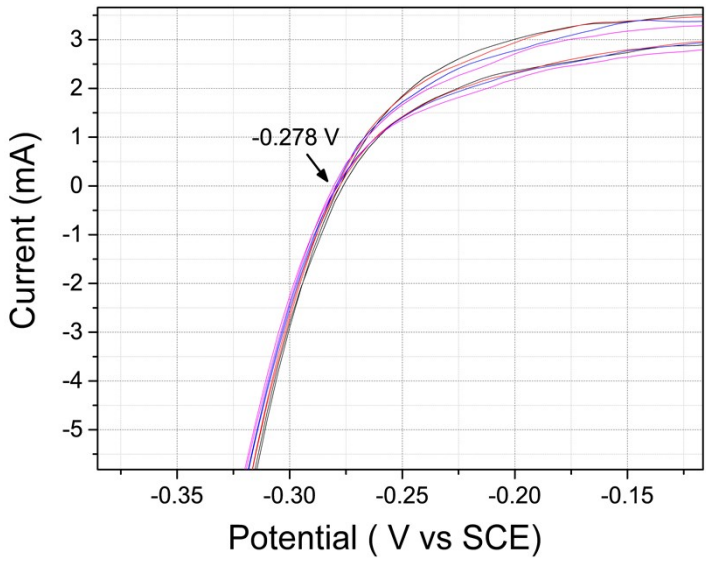


**Fig. E1** CV curves for the potential of reference electrode (SCE), obtained at a scan rate of 2 mV $s^{-1}$, in the high-purity $H_2$ saturated 0.5 M $H_2SO_4$ electrolyte with a Pt wire as the working electrode.

The applied potentials (E) reported in our work were referenced to the reversible hydrogen electrode (RHE) through standard calibration. As a first step, we calibrate the potential of SCE *vs*. standard hydrogen electrode (SHE). Cyclic voltammetry (CV) curves were obtained at a scan rate of 2 mV $s^{-1}$, in the high-purity $H_2$ saturated 0.5 M $H_2SO_4$ electrolyte with a Pt wire as

the working electrode, as shown in **Fig. E1**. The average value of the potential at which the current crossed at zero was -0.278 V. Therefore $E_{SCE}$ = 0.278 V, since E (= 0 *vs*. SHE) - $E_{SCE}$ = -0.278 V.

In 0.5 M $H_2SO_4$ electrolyte (pH 0), E (*vs*. RHE) = E (*vs*. SCE) + $E_{SCE}$ (= 0.278 V) + 0.0592 pH = E (*vs.* SCE) + 0.278 V. The overpotential (η) was defined as E (*vs.* RHE). 4 mg TMD nanosheet sample was mixed with 1 mg carbon black (Vulcan XC-72) dispersed in Nafion (20 μL) and isopropyl alcohol (0.98 mL). The catalyst materials (0.39 mg $cm^{-2}$) were deposited on a glassy carbon rotating disk electrode (RDE, area = 0.1641 $cm^2$, Pine Instrument), and a rotation speed of 1600 rpm was used for the linear sweep voltammetry (LSV) measurements. The Pt/C (20 wt.% Pt in Vulcan carbon black, Sigma-Aldrich) tested as reference sample using the same procedure. The LSV curve of each sample was obtained by averaging first 8-10 scans. For chronoamperometric stability test, we fabricated the electrode by depositing the samples (1 mg $cm^{-2}$) on 1 × 1 $cm^2$ area of hydrophilic/water proof carbon cloth (WIZMAC Co., thickness = 0.35 mm, through-plane resistance = 1 mΩ) that was cut with a size of 1 × 3 $cm^2$.

Electrochemical impedance spectroscopy (EIS) measurements were carried out for the electrode in an electrolyte by applying an AC voltage of 10 mV in the frequency range of 100 kHz to 0.1 Hz at a bias voltage of -0.1 V (*vs*. RHE). To measure double-layer capacitance *via* CV, a potential range in which no apparent Faradaic processes occur was determined from static CV. This range is 0.1–0.2 V. All measured current in this non-Faradaic potential region

is assumed to be due to double-layer capacitance. The charging current, $i_c$, is then measured from CVs at multiple scan rates. The working electrode was held at each potential vertex for 10 s before beginning the next sweep. The charging current density ($i_c$) is equal to the product of the scan rate (ν) and the electrochemical double-layer capacitance ($C_{dl}$), as given by equation $i_c = \nu C_{dl}$. The difference ($\Delta J_{0.15}$) between the anodic charging and cathodic discharging currents measured at 0.15 V (*vs*. RHE) was used for $i_c$. Thus, a plot of $\Delta J_{0.15}$ as a function of ν yields a straight line with a slope equal to $2 \times C_{dl}$. The scan rates were 100–200 mV $s^{-1}$.

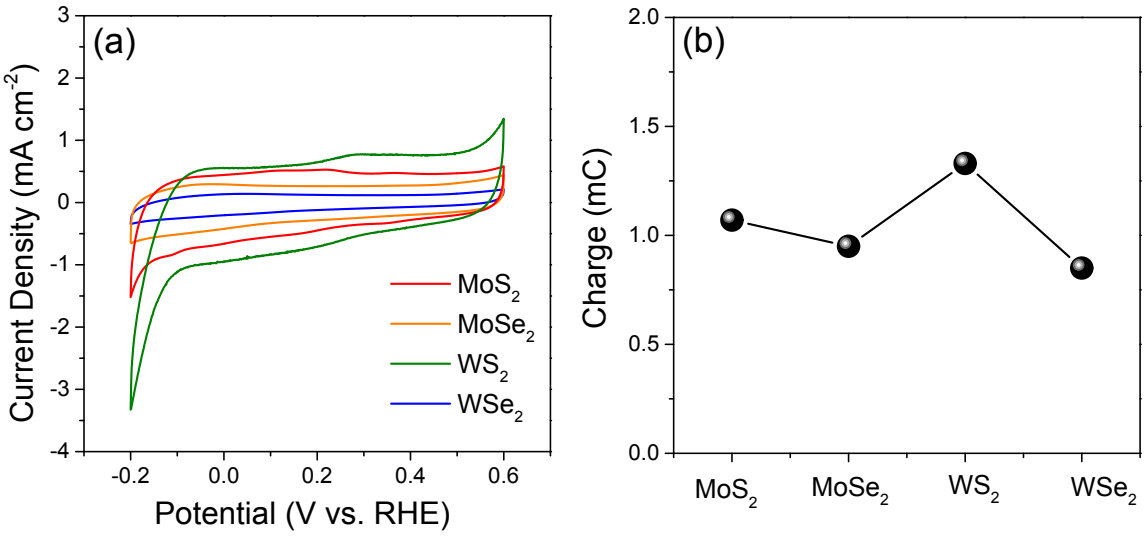


**Fig. E2** (a) CV curves of TMD samples measured at a scan rate of 50 mV $s^{-1}$, in 0.1 M phosphate buffer solution (pH 7, range = -0.2 ~ 0.6 V vs. RHE). (b) Charge integrated from the CV curves of each sample.

The active site density and turnover frequency (TOF) have been estimated as follows. It should be emphasized that since the nature of the active sites of the catalyst is not clearly understood yet and the real surface area for the nanostructured heterogeneous catalyst is hard

to accurately determine, the following result is really just an estimation. The active sites are determined by the charge (Q) integrated from the CV curves (**Fig. E2**), which was obtained in 0.1 M phosphate buffer solution (pH 7, Range = -0.2 ~ 0.6 V vs. RHE). While it is difficult to assign the observed peaks to a given redox couple, the integrated charge over the whole potential range should be proportional to the total number of active sites. The formula employed to find the number of electrochemically active sites ($m$) is given by $m = \frac{Q}{2e}$, where Q is charge in Coulomb and the factor ½ is number of electrons taking part in oxidation/reduction process.[S1,S2]

The TOF can be caculated from the total number of hydrogen gas ($H_2$) molecules ($n_{H2}$) turns overs at a required potential as follows. TOF = $n_{H2}/m$ = $J$ (mA cm$^{-2}$) × 3.12 × 10$^{15}$ ($H_2$ s$^{-1}$ per mA cm$^{-2}$) × electrode area (= 0.1641 cm$^2$)/$m$, where $n_{H2}$ was calculated from the current density ($J$) according to $n_{H2}$ = $J$ (mA cm$^{-2}$)/1000 mA × 1 (C s$^{-1}$) × 1 mol e$^-$/96486 C × 1 mol $H_2$/2 mol e$^-$ × 6.022 × 10$^{23}$ $H_2$ molecules/1 mol $H_2$ × electrode area = $J$ (mA cm$^{-2}$) × 3.12 × 10$^{15}$ ($H_2$ s$^{-1}$) × electrode area (= 0.1641 cm$^2$). We summarized the results in **Table E**.

**Table E**. TOF of samples at η = 0.2 V, calculated using the density of surface active ($m$).

| Samples | $J$ (mA cm$^{-2}$) at 0.2 V | $n_{H2}$ | $Q$ (mC) | $m$ | TOF ($H_2$ s$^{-1}$) |
|---|---|---|---|---|---|
| $MoS_2$ | 14.72 | 7.53 × 10$^{15}$ | 1.07 | 3.33 × 10$^{15}$ | 2.25 |
| $MoSe_2$ | 25.42 | 1.30 × 10$^{16}$ | 0.95 | 2.96 × 10$^{15}$ | 4.39 |
| $WS_2$ | 42.02 | 2.15 × 10$^{16}$ | 1.33 | 4.15 × 10$^{15}$ | 5.18 |
| $WSe_2$ | 9.46 | 4.84 × 10$^{15}$ | 0.85 | 2.65 × 10$^{15}$ | 1.82 |

**Table S1**. Comparison of the performance of solar water-splitting PEC cells using Si-TMD based cathode.

| Year | Ref. No.[a] | Materials (Electrolyte) | $V_{OC}$ (V vs. RHE)[b] | $J_{SC}$ (mA/cm$^2$)[c] | $J_{max}$ (mA/cm$^2$)[d] |
|---|---|---|---|---|---|
| 2011 | S3 [11] | $Mo_3S_4$/Si pillars (1.0 M $HClO_4$) | 0.15 | 8 | 14 at -0.6 V |
| 2012 | S4 [25] | Si-NW@$MoS_2$ (1.0 M $Na_2SO_4$) | 0.1 | 1 | 10 at -0.4 V |
| 2014 | S5 [26] | 1T-$MoS_2$/Si (0.5 M $H_2SO_4$) | 0.25 | 17.6 | 26.7 at -0.4 V |
| 2015 | S6 [17] | $MoS_xCl_y$/Si Micropyramid (0.5 M $H_2SO_4$) | 0.41 | 43.0 | 44 at -0.1 V |
| | S7 [27] | $MoS_2/TiO_2/n^+$p-Si NWs (0.5 M $H_2SO_4$) | 0.3 | 15 | 25 at -0.37 V |
| 2016 | S8 [28] | $MoS_2$/p-Si (0.5 M $H_2SO_4$) | 0.17 | 24.6 | 40 at -1.0 V |
| 2017 | S9 [29] | Co-doped $MoS_2$/p-Si Microwire (0.5 M $H_2SO_4$) | 0.192 | 17.2 | 30 at -0.2 V |
| | S10 [30] | $MoS_2$/Si-NW (0.5 M $H_2SO_4$) | 0.25 | 14.3 | 16.5 at -0.7 V |
| | S11 [31] | ALD $MoS_2$/Si (0.5 M $H_2SO_4$) | 0.23 | 21.7 | 31 at -0.2 V |
| | S12 [32] | $MoS_2/Al_2O_3/n^+$ p-Si (1 M $HClO_4$) | 0.4 | 34 | 35.6 at -0.4 V |
| | S13 [33] | Si-$MoS_2$ (0.5 M $H_2SO_4$) | 0.31 | 14 | 15.3 at -0.3 V |
| 2018 | S14 | p-Si/$SiO_x$/1T-2H $MoS_2$ (0.5 M $H_2SO_4$) | 0.35 | ~30 | 30 at -0.5 V |
| | S15 [34] | $MoSe_2/n^+$p-Si (1 M $HClO_4$) | 0.4 | 29.3 | 30.7 at -1.0 V |
| | S16 | 3D $MoS_2/TiO_2$/p-Si (0.5 M $H_2SO_4$) | 0.35 | 28 | 36 at -1.2 V |
| | S17 | Ag@Si/$MoS_2$ (0.5 M $H_2SO_4$) | 0.17 | ~5 | 33.4 at -0.4 V |
| | S18 [35] | Co-W-S/$n^+$p-S (1.0 M $HClO_4$) | 0.32 | 30.1 | 36 at -0.6 V |
| 2019 | S19 [36] | Si/GaP–$TiO_2$–$MoS_2$ (1.0 M $HClO_4$) | 0.46 | 0.95 | 1 at -0.8 V |
| | S20 [37] | $MoS_2/WS_2/WSe_2$/p-Si (0.5 M $H_2SO_4$) | 0.14 | 11.54 | 35 at -1.0 V |
| | S21 [38] | $WS_2$/p-Si (0.5 M $H_2SO_4$) | 0.1 | 9.8 | 36 at -0.4V |
| 2020 | S22 [39] | $MoS_2/Ni_3S_2$/Si (1 M KOH) | 0.54 | 41.5 | 41.5 at 0 V |
| | Our work | $MoS_2$-Si NW (0.5 M $H_2SO_4$) | 0.2 | 30 | 32 at -0.2V |

[a] The number in bracket is the reference number in the main text.; [b] $J_{SC}$: short circuit current (current density at 0 V vs. RHE); [c] $V_{OC}$: open circuit voltage; [d] maximum current density.

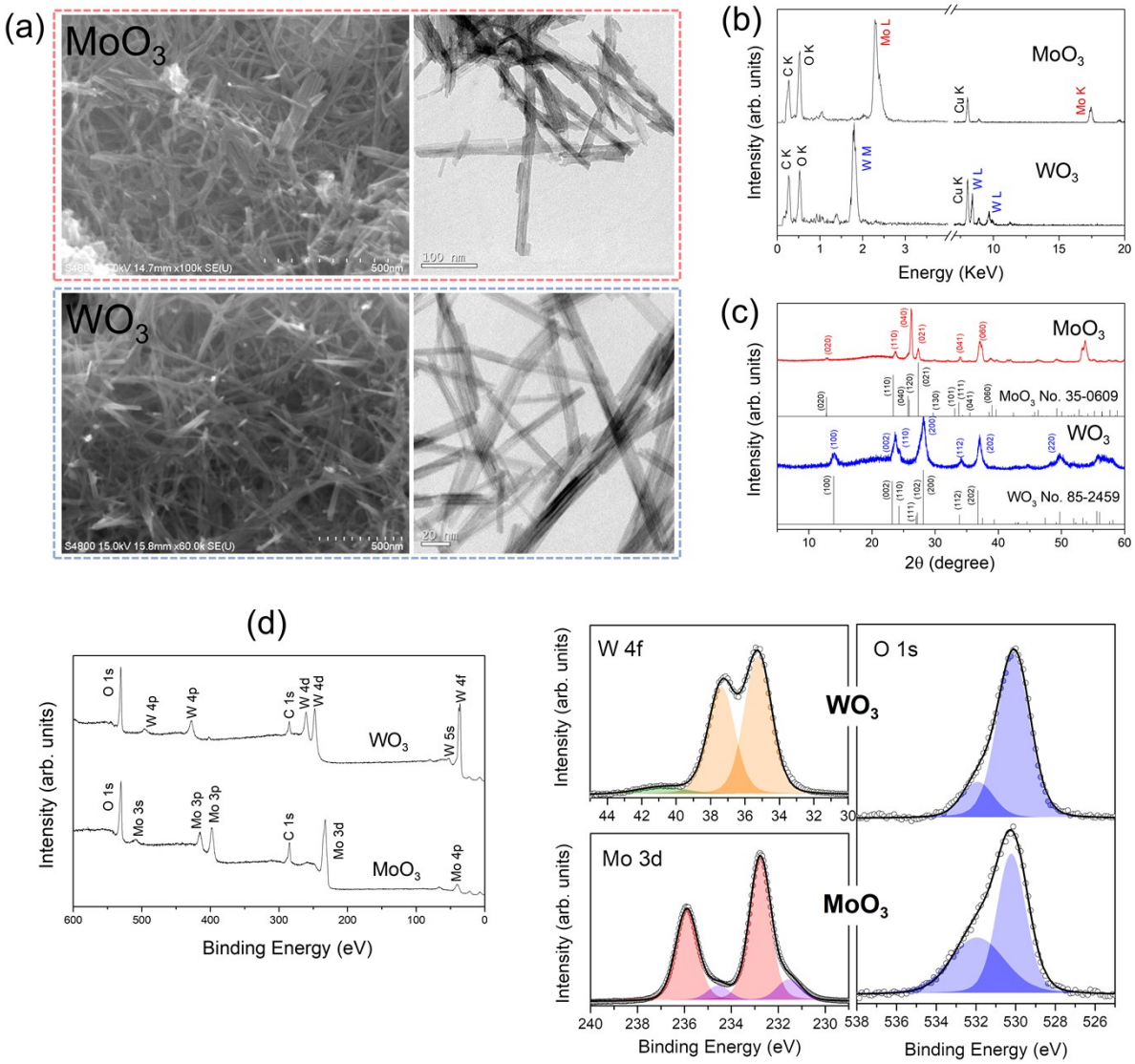


**Fig. S1** (a) SEM and HRTEM images, (b) EDX spectrum, (c) XRD pattern, and (d) XPS data of wire-like $MoO_3$ and $WO_3$ nanoparticles.

The SEM and HRTEM images revealed the nanowire morphology with the diameter of 10-20 nm. The EDX spectrum shows the Mo and W composition. The XRD peaks were matched to those of orthorhombic phase $MoO_3$ (JCPDS No. 35-0609, Pbnm, $a$ = 3.963 Å, $b$ = 13.85 Å, $c$ = 3.696 Å) and hexagonal phase $WO_3$ (JCPDS No. 85-2459, $P6_3/mcm$, $a$ = 7.324 Å, $c$ = 7.662 Å). The XPS survey scan and fine-scanned Mo 3$d$, W 4$f$, and O 1s peaks shows the successful synthesis of oxide form. The Mo $3d_{5/2}$ and W $4f_{7/2}$ peaks blueshift significantly from the position of the metal phase peak ($Mo^0$ $3d_{5/2}$ at 228.0 eV and $W^0$ $4f_{7/2}$ at 31.4 eV), due to the cation form. The O 1$s$ peak redshifts from the position of the neutral peak ($O^0$ at 532 eV) due to the anion form. A laboratory-based spectrometer was used with a photon energy of 1486.6 eV (Al Kα).

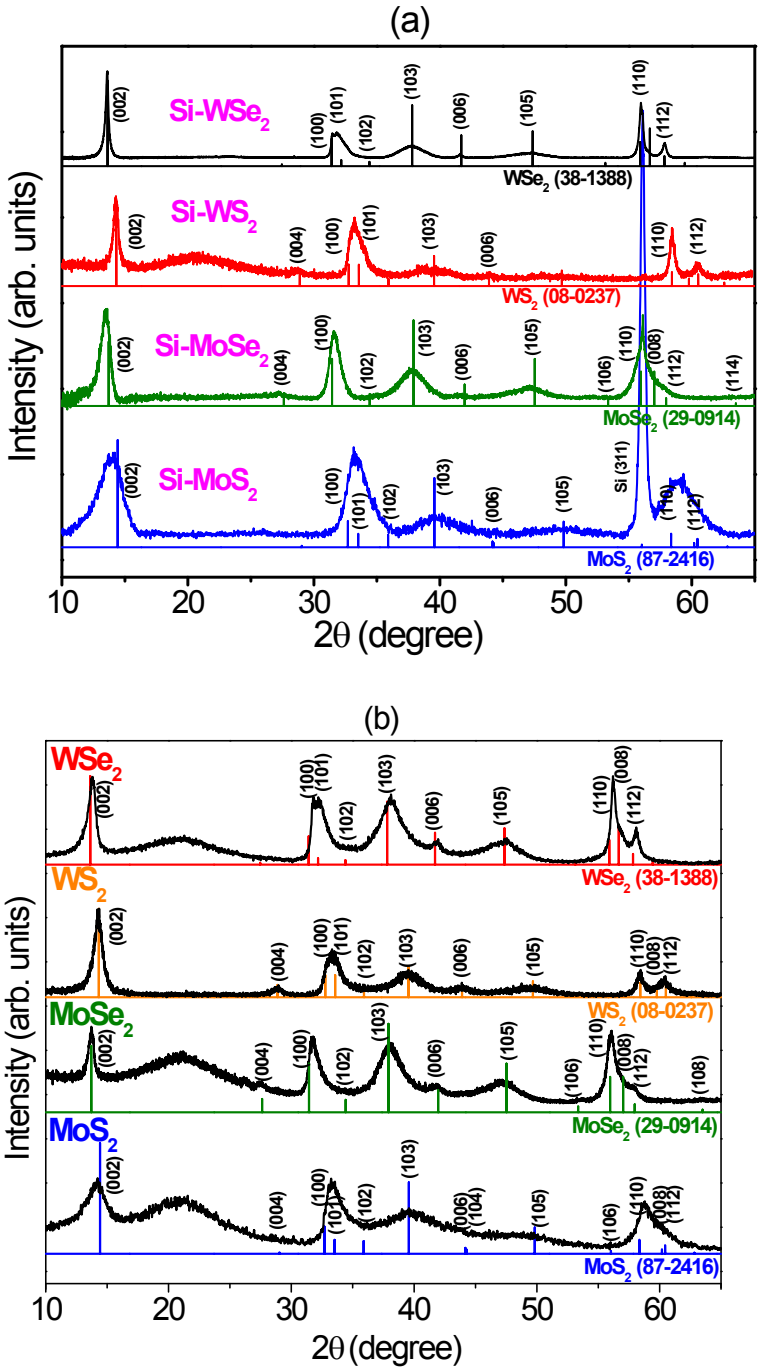


**Fig. S2** XRD pattern of (a) Si-$MoS_2$, Si-$MoSe_2$, Si-$WS_2$, and Si-$WSe_2$ NW samples and (a) free-standing $MoS_2$, $MoSe_2$, $WS_2$, and $WSe_2$ nanosheets. The peaks of the samples were referenced to those of hexagonal phase $MoS_2$ (JCPDS No. 87-2416, $P6_3/mmc$, $a$ = 3.160 Å, $c$ = 12.290 Å), $MoSe_2$ (JCPDS No. 29-0914, $P6_3/mmc$, $a$ = 3.287 Å, $c$ = 12.925 Å), $WS_2$ (JCPDS No. 08-0237, $P6_3/mmc$, $a$ = 3.154 Å, $c$ = 12.362 Å). $WSe_2$ (JCPDS No. 38-1388, $P6_3/mmc$, $a$ = 3.285 Å, c = 12.982 Å). Si (311) peak at 56.5° is assigned using the cubic phase Si (JCPDS No. 80-0018, F3m, $a$ = 5.392 Å). The broad peak at 2θ = 21° originated from the sample holder that made of quartz. If the amount of the sample was not enough to cover the holder, the holder peak appears.

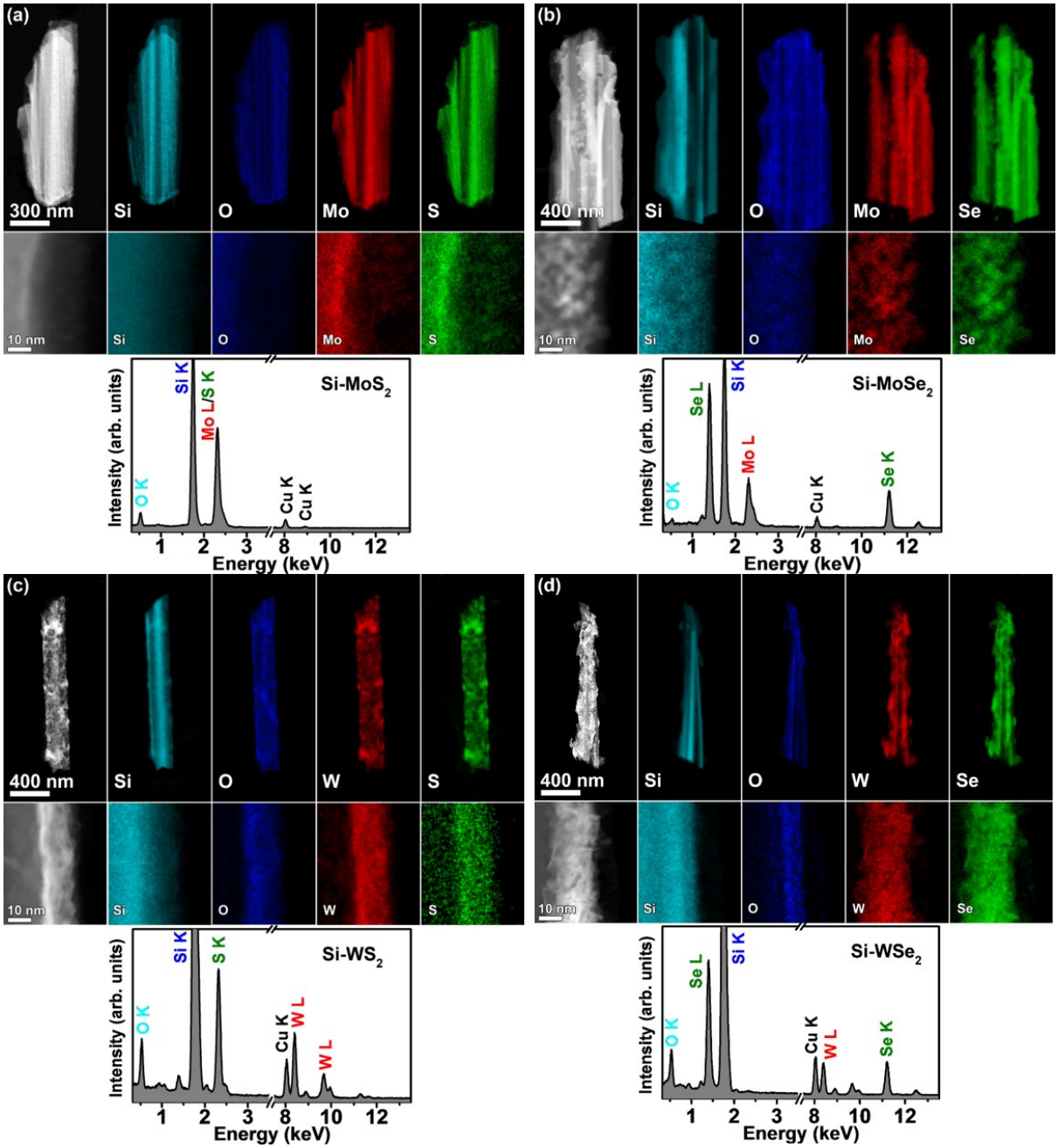


**Fig. S3** HAADF STEM image, EDX elemental mapping of Si, O, Mo (or W), and S (or Se) elements, and corresponding EDX spectrum for (a) Si-$MoS_2$, (b) Si-$MoSe_2$, (c) Si-$WS_2$, and (d) Si-$WSe_2$. Two sets of EDX elemental mapping correspond to the whole NW (top) and the magnified region for the Si-TMD interface (bottom). The [S]/[Mo] = 2.0 for $MoS_2$, [Se]/[Mo] = 1.91 for $MoSe_2$, [S]/[W] = 1.85 for $WS_2$, and [Se]/[W] = 1.68 for $WSe_2$.

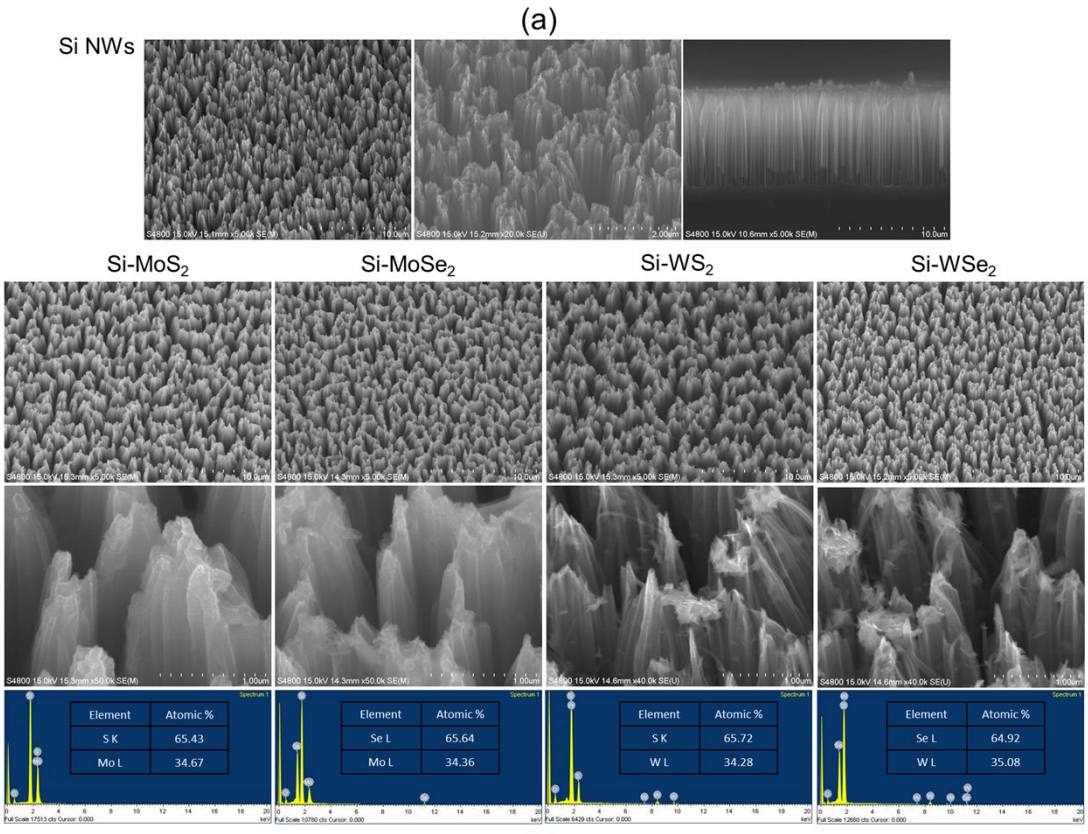


| | $MoS_2$ | $MoSe_2$ | $WS_2$ | $WSe_2$ |
|---|---|---|---|---|
| SEM/EDX of samples | 1.88 | 1.91 | 1.91 | 1.85 |
| XPS of samples | 1.85 | 1.95 | 1.93 | 1.89 |
| TEM/EDX of samples | 2.0 | 1.91 | 1.85 | 1.68 |
| Average | 1.85* | 1.92 | 1.90 | 1.80 |

**Fig. S4** (a) SEM EDX data of the samples. (b) [X]/[M] ratio of $MoS_2$, $MoSe_2$, $WS_2$, and $WSe_2$ nanosheets and corresponding bulk powders. In the EDX spectrum, Mo L shell and S K shell peaks are overlapped so that the [S]/[Mo] is inaccurate. Therefore, we used only XPS data to obtain the ratio for $MoS_2$. SEM EDX and XPS data shows that the average value of $MoS_2$, $MoSe_2$, $WS_2$, and $WSe_2$ is [S]/[Mo] = 1.85, [Se]/[Mo] = 1.92, [S]/[W] = 1.90, and [Se]/[W] = 1.81, respectively.

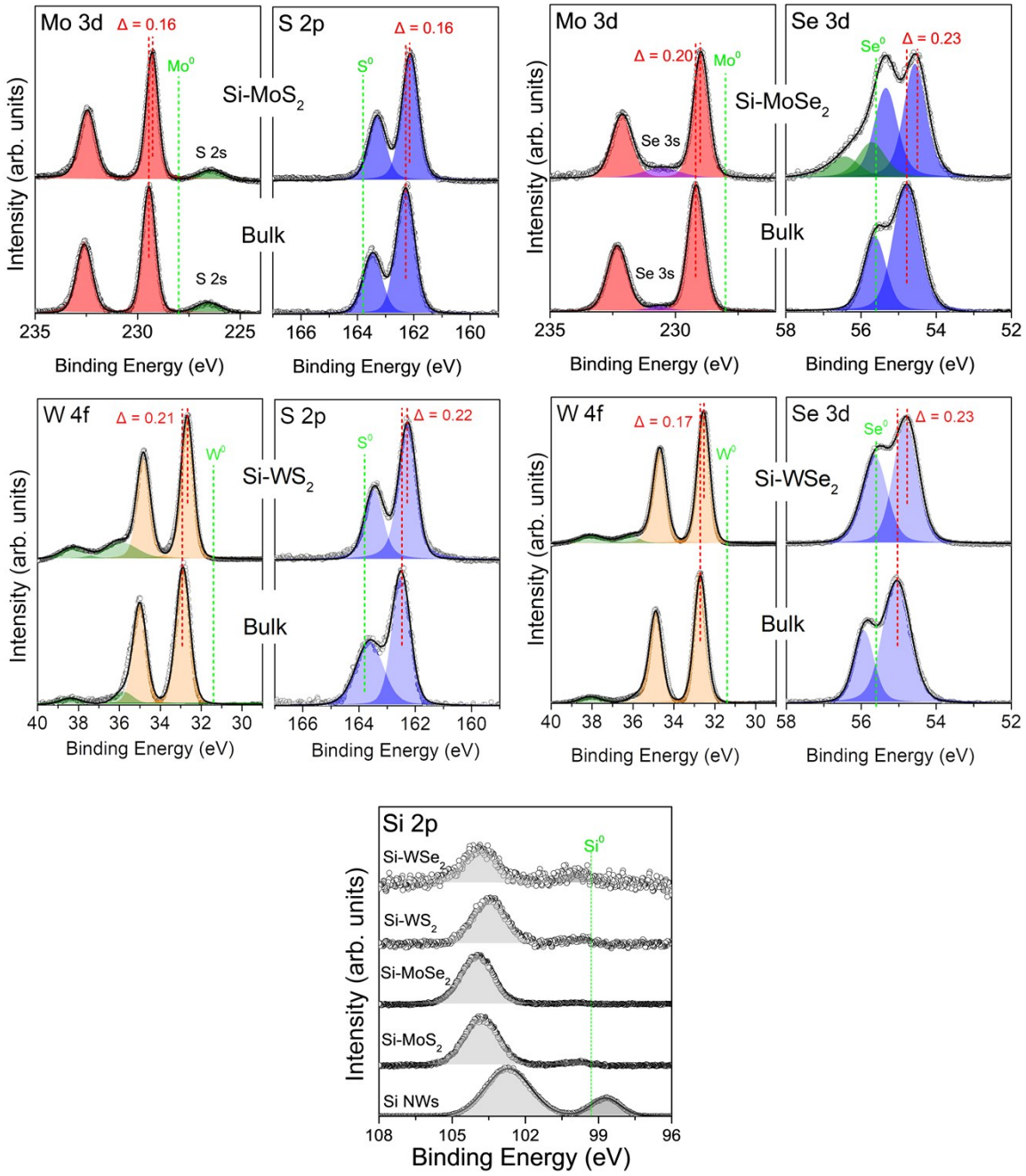


**Fig. S5** Fine-scanned XPS data of Mo 3*d*, W 4*f*, S 2*p*, Se 3*d*, and Si 2*p* peaks of bulk powders and Si-TMD samples. The data points (open circles) are fitted by Voigt functions. The position of the metal phase peak ($Mo^0$ $3d_{5/2}$ at 228.0 eV, $W^0$ $4f_{7/2}$ at 31.4 eV, $S^0$ $2p_{3/2}$ at 164.0 eV, $Se^0$ $3d_{5/2}$ at 55.6 eV, and $S^0$ 2*p* at 99.3 eV) is marked by a vertical dotted line to delineate the blueshift or redshift. We used the 8A1 beam line of the PLS with a photon energy of 600 eV, So the peak position and shapes are different from those shown in Fig. S9.

Peak position (in eV) is summarized in the following table, where the $\Delta E_M$ represents the Mo or W peak red shift of the sample relative to that of the bulk, and $\Delta E_X$ corresponds to the S

or Se peaks. The redshift of the XPS binding energies could be attributed to the states at the nearest $E_F$, which are correlated with the more metallic phase. The chalcogen vacancy makes the sample more metallic. The XPS data consistently show that the TMD nanosheets are more metallic than the bulk phase. The shifts are similar for all samples, which is correlated with the concentration of chalcogen vacancies (5-10%). In the case of Si-$MoSe_2$, the peak was resolved into four bands: two Se1 bands (at 54.6 and 55.4 eV) for the $Se^{2-}$ of Mo-Se bonding structures, and two blue Se2 bands (at 55.7 and 56.5 eV) for the bridge ($Se_2^{2-}$) anions at the defects. The Si and Si-O peaks of Si NWs appears at 98.6 and 102.8 eV. The Si-TMD samples show a blueshift to 99.8 and 104 eV, respectively.

| | | Mo $3d_{5/2}$ | W $4f_{7/2}$ | S $2p_{3/2}$ | Se $3d_{5/2}$ | $\Delta E_M$ | $\Delta E_X$ |
|---|---|---|---|---|---|---|---|
| $MoS_2$ | Bulk | 229.45 | | 162.29 | | 0.16 | 0.16 |
| | Sample | 229.29 | | 162.13 | | | |
| $MoSe_2$ | Bulk | 229.18 | | | 54.76 | 0.20 | 0.23 |
| | Sample | 229.98 | | | 54.53 | | |
| $WS_2$ | Bulk | | 32.89 | 162.49 | | 0.21 | 0.22 |
| | Sample | | 32.68 | 162.27 | | | |
| $WSe_2$ | Bulk | | 32.71 | | 55.01 | 0.17 | 0.23 |
| | Sample | | 32.54 | | 54.78 | | |

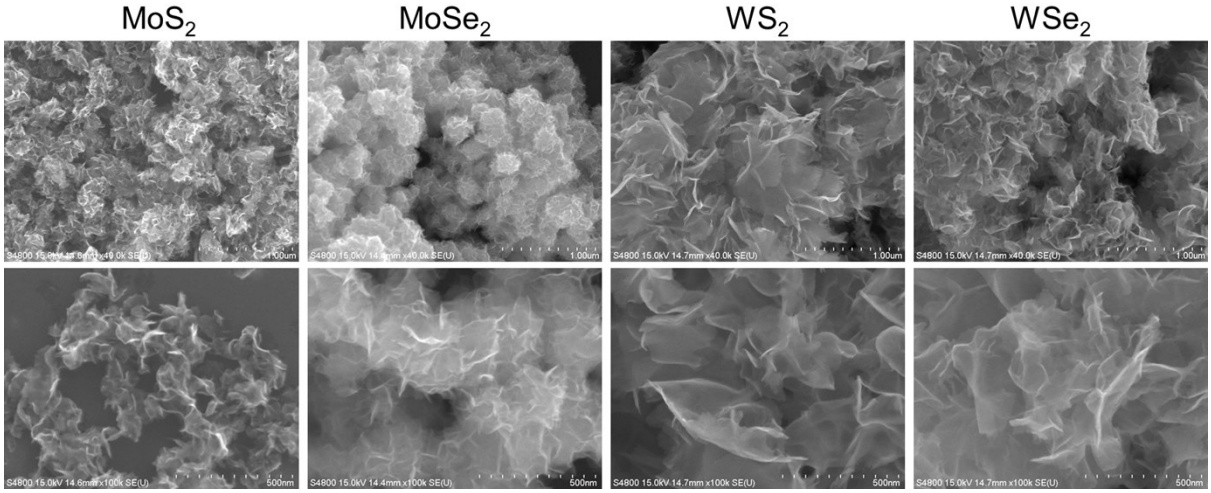


**Fig. S6** SEM images of freestanding $MoS_2$, $MoSe_2$, $WS_2$, and $WSe_2$ nanosheets.

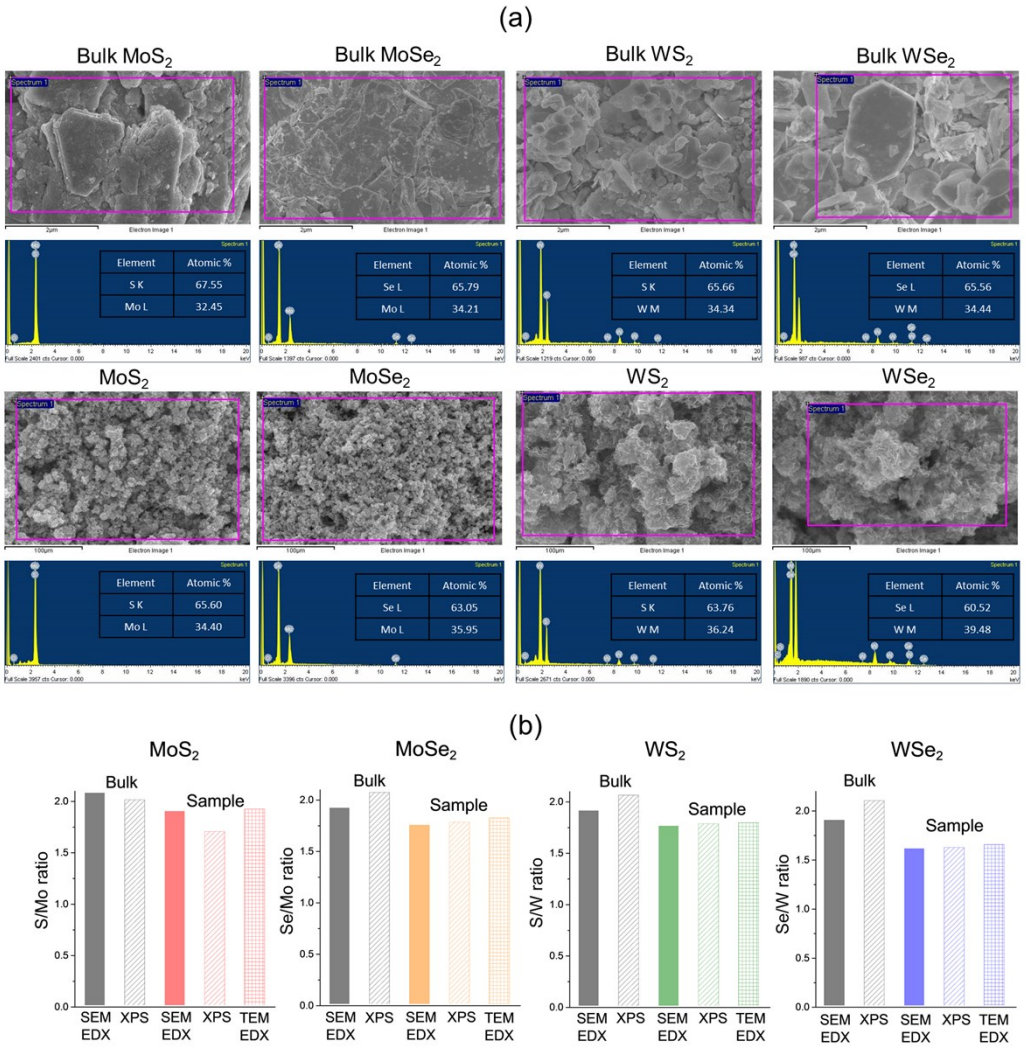


| | $MoS_2$ | $MoSe_2$ | $WS_2$ | $WSe_2$ |
|---|---|---|---|---|
| SEM EDX of bulk | 2.08 | 1.92 | 1.91 | 1.90 |
| XPS of bulk | 2.01 | 2.07 | 2.06 | 2.10 |
| Average | 2.05 | 2.0 | 2.0 | 2.0 |
| SEM/EDX of samples | 1.90 | 1.76 | 1.75 | 1.61 |
| XPS of samples | 1.69 | 1.78 | 1.77 | 1.62 |
| TEM/EDX of samples | 1.92 | 1.82 | 1.79 | 1.65 |
| Average | 1.7* (XPS) | 1.8 | 1.8 | 1.6 |

**Fig. S7** (a) SEM EDX data of the commercially available bulk powders ($MoS_2$ 99%, $MoSe_2$ 99%, $WS_2$ 99.8%, and $WSe_2$ 99.8%, purchased from Alfa Aesar) and the $MoS_2$, $MoSe_2$, $WS_2$, and $WSe_2$ nanosheets. (b) [X]/[M] ratio of $MoS_2$, $MoSe_2$, $WS_2$, and $WSe_2$ nanosheets and corresponding bulk powders. In the EDX spectrum, Mo L shell and S K shell peaks are overlapped so that the [S]/[Mo] is inaccurate. Therefore, we used only XPS data to obtain the ratio for $MoS_2$. SEM EDX, XPS. TEM EDX data shows that the average value of [X]/[M] ratio of bulk powders is 2, while that of $MoS_2$, $MoSe_2$, $WS_2$, and $WSe_2$ is [S]/[Mo] = 1.7, [Se]/[Mo] = 1.8, [S]/[W] = 1.8, and [Se]/[W] = 1.6, respectively.

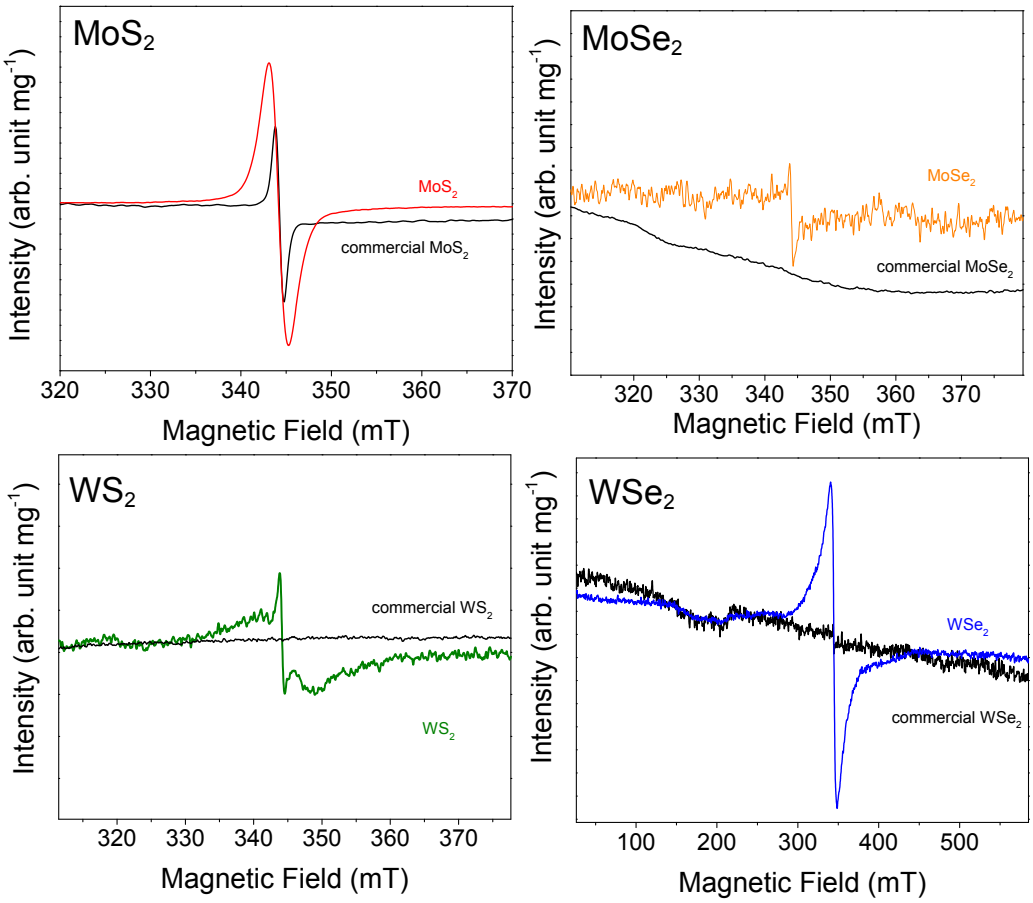


**Fig. S8** Electron spin (or paramagnetic) resonance (ESR or EPR) spectra for $MoS_2$, $MoSe_2$, $WS_2$, and $WSe_2$ nanosheets and corresponding commercially available bulk powders ($MoS_2$ 99%, $MoSe_2$ 99%, $WS_2$ 99.8%, and $WSe_2$ 99.8%, purchased from Alfa Aesar).

ESR measurements were performed on a Bruker EMX-Plus spectrometer at room temperature. Ten milligrams of as-prepared samples were loaded in a quartz tube. The microwave frequency $\nu$ was 9.64 GHz (X-band), and the $g$-factor was calculated as $h\nu = g \times \mu_B \times B$, where $\mu_B$ and B are the Bohr magneton and magnetic field, respectively. Bulk powders samples have no signal except $MoS_2$. In contrast, all nanosheet samples exhibit a S shape signal (per mg) at 344 mT ($g$ = 2.00), due to the S or Se vacancies. The $MoS_2$ and $WSe_2$ exhibit a stronger S shaped signal than $MoSe_2$ and $WS_2$, which is correlated with the higher concentration of chalcogen vacancies.

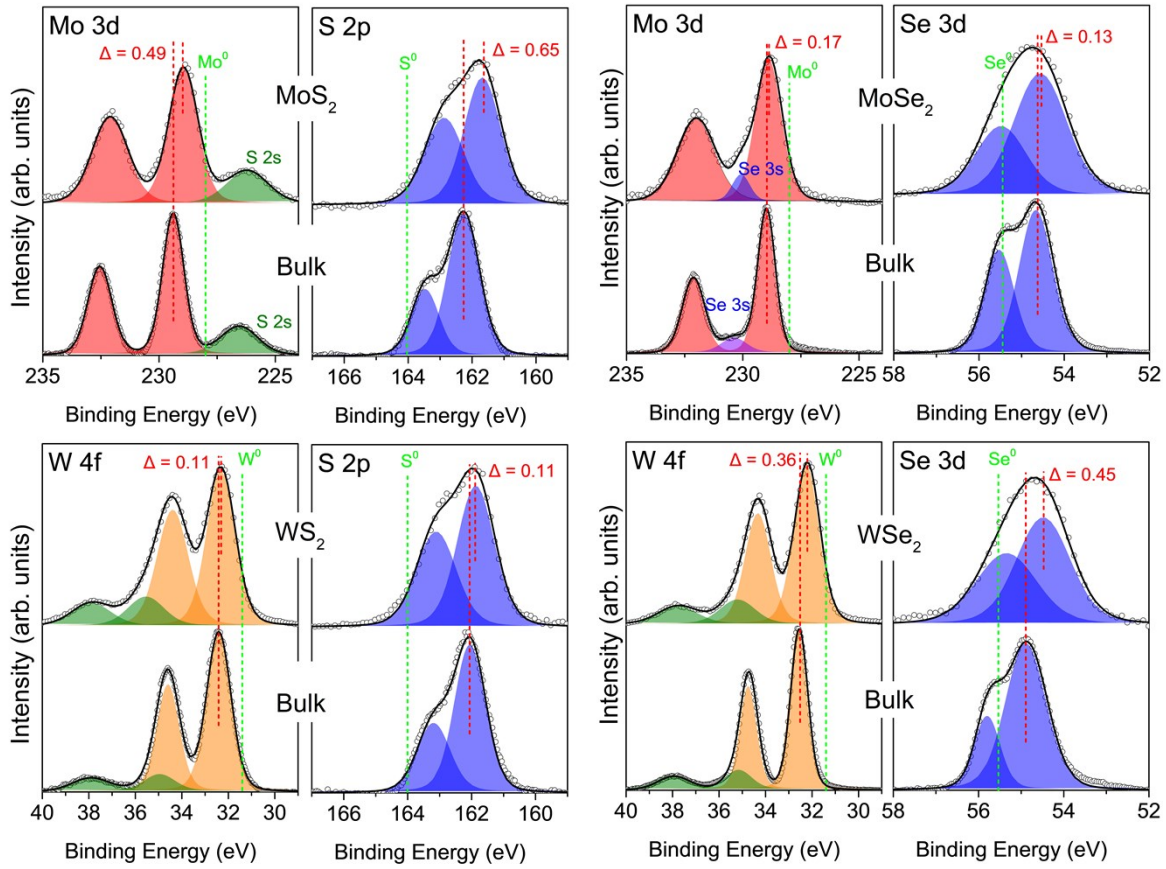


**Fig. S9** Fine-scanned XPS data of Mo 3*d*, W 4*f*, S 2*p*, and Se 3*d* peaks of bulk and freestanding nanosheets. The data points (open circles) are fitted by Voigt functions. The position of the metal phase peak ($Mo^0$ $3d_{5/2}$ at 228.0 eV, $W^0$ $4f_{7/2}$ at 31.4 eV, $S^0$ $2p_{3/2}$ at 164.0 eV, and $Se^0$ $3d_{5/2}$ at 55.6 eV) is marked by a vertical dotted line to delineate the blueshift or redshift. A laboratory-based spectrometer was used with a photon energy of 1486.6 eV (Al Kα).

Peak position is summarized in the following table, where the $\Delta E_M$ represents the Mo or W peak redshift (in eV) of the sample relative to that of the bulk, and $\Delta E_X$ corresponds to the redshift of S or Se peaks. The redshift of the XPS binding energies could be attributed to the states at the nearest $E_F$, which are correlated with the more metallic phase. The chalcogen vacancy makes the sample more metallic. The XPS data consistently show that the TMD nanosheets are more metallic than the bulk phase. The magnitude of redshift is larger for $MoS_2$ and $WSe_2$ compared to $MoSe_2$ and $WS_2$, due to the higher concentration of chalcogen vacancies.

| | | Mo $3d_{5/2}$ | W $4f_{7/2}$ | S $2p_{3/2}$ | Se $3d_{5/2}$ | $\Delta E_M$ | $\Delta E_X$ |
|---|---|---|---|---|---|---|---|
| $MoS_2$ | Bulk | 229.39 | | 162.29 | | 0.49 eV | 0.65 eV |

| | | | | | | | |
|---|---|---|---|---|---|---|---|
| | Sample | 228.90 | | 161.64 | | | |
| $MoSe_2$ | Bulk | 229.98 | | | 54.63 | 0.17 eV | 0.11 eV |
| | Sample | 229.81 | | | 54.50 | | |
| $WS_2$ | Bulk | | 32.41 | 162.02 | | 0.11 eV | 0.11 eV |
| | Sample | | 32.30 | 161.86 | | | |
| $WSe_2$ | Bulk | | 32.56 | | 54.87 | 0.36 eV | 0.45 eV |
| | Sample | | 32.20 | | 54.42 | | |

(a)

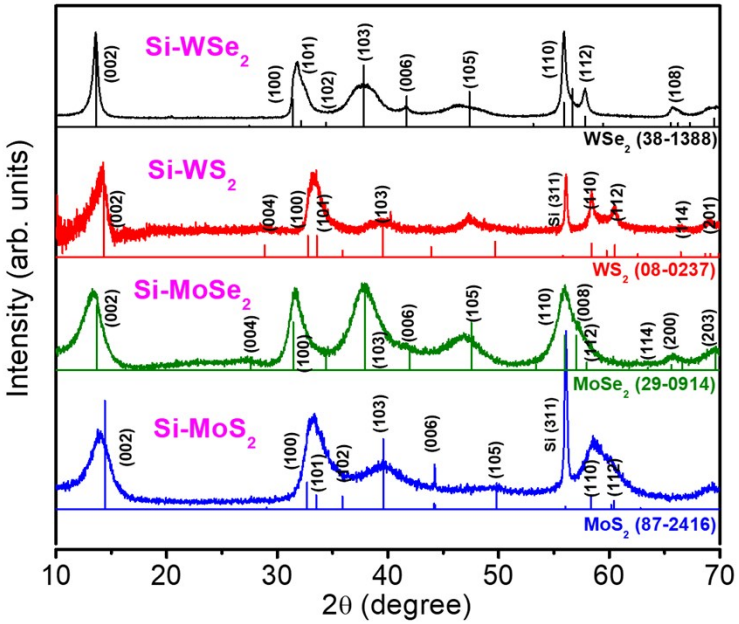
Si-WSe2
(002)
(100)
(101)
(102)
(103)
(006)
(105)
(110)
(112)
(108)
WSe2 (38-1388)
Si-WS2
(002)
(004)
(100)
(101)
(103)
Si (311)
(110)
(112)
(114)
(201)
WS2 (08-0237)
Si-MoSe2
(002)
(004)
(100)
(103)
(006)
(105)
(110)
(008)
(112)
(114)
(200)
(203)
MoSe2 (29-0914)
Si-MoS2
(002)
(100)
(101)
(102)
(103)
(006)
(105)
Si (311)
(110)
(112)
MoS2 (87-2416)
Intensity (arb. units)
10
20
30
40
50
60
70
2θ (degree)

(b)

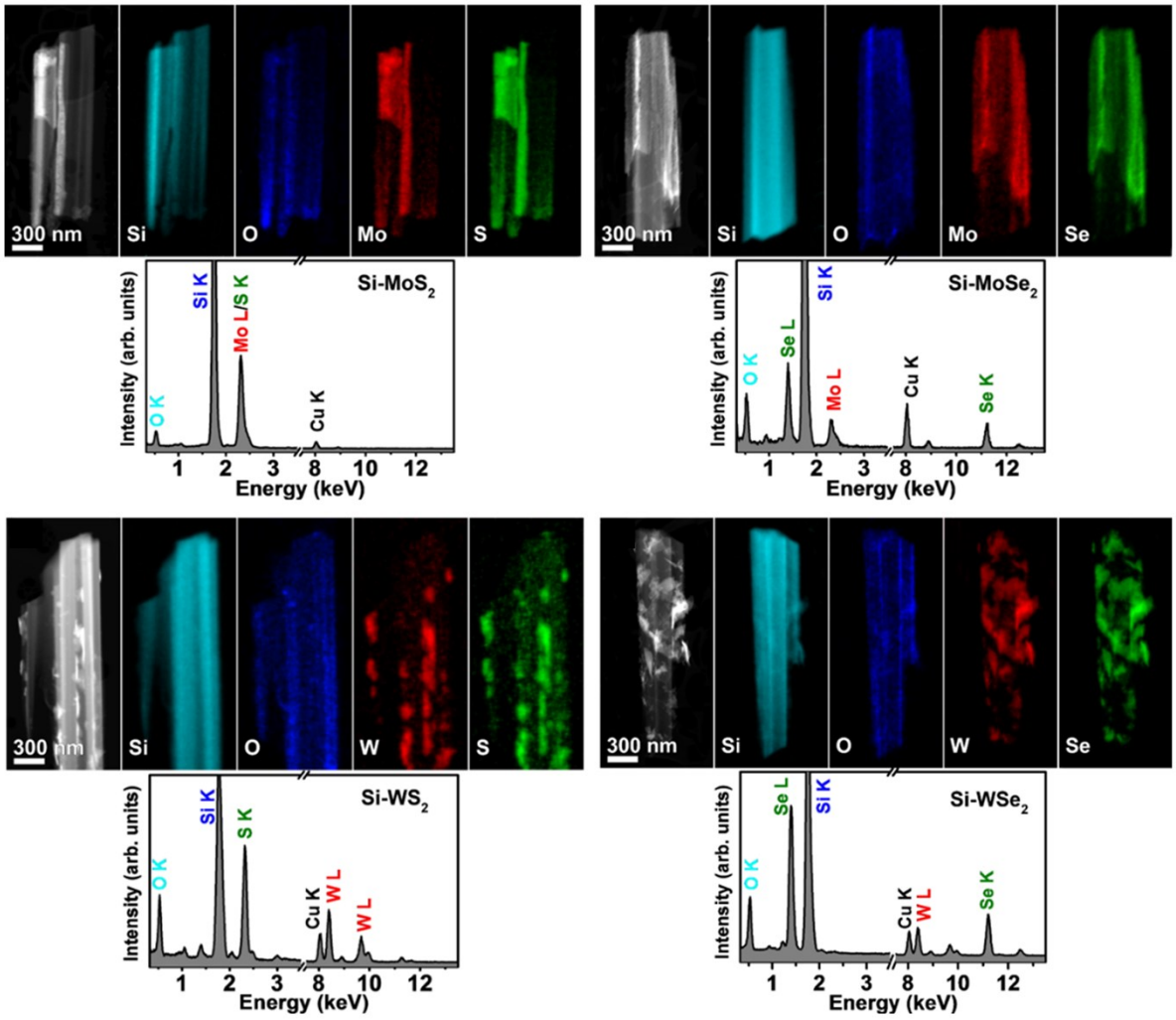
300 nm
Si
O
Mo
S
Si-MoS2
O K
Si K
Mo L/S K
Cu K
Intensity (arb. units)
1
2
3
8
10
12
Energy (keV)
300 nm
Si
O
Mo
Se
Si-MoSe2
O K
Se L
Si K
Mo L
Cu K
Se K
Intensity (arb. units)
Energy (keV)
300 nm
Si
O
W
S
Si-WS2
O K
Si K
S K
Cu K
W L
W L
Intensity (arb. units)
Energy (keV)
300 nm
Si
O
W
Se
Si-WSe2
O K
Se L
Si K
Cu K
W L
Se K
Intensity (arb. units)
Energy (keV)

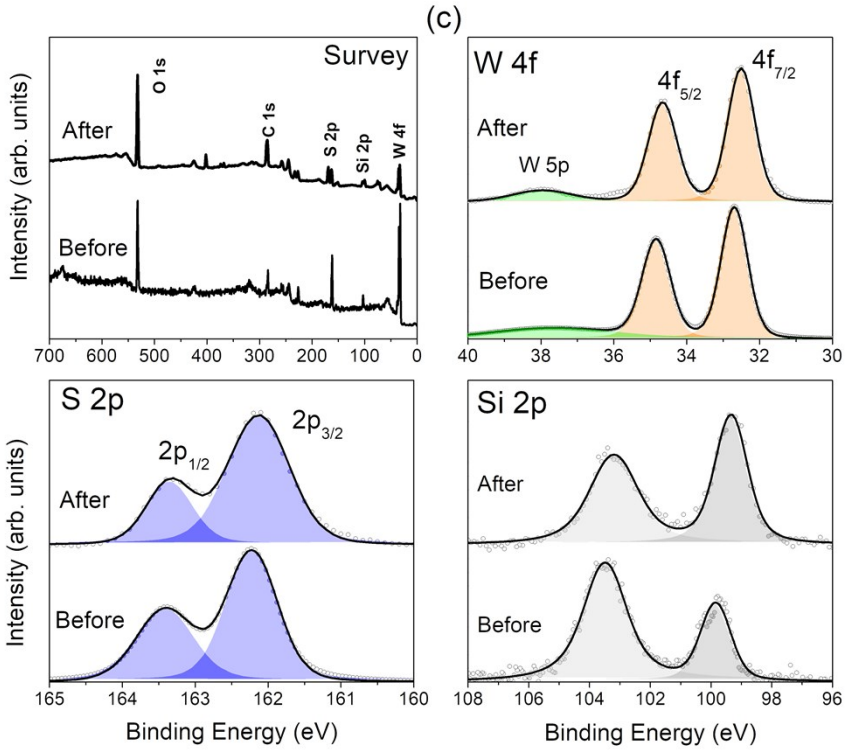


**Fig. S10** (a) XRD pattern of Si-$MoS_2$, Si-$MoSe_2$, Si-$WS_2$, and Si-$WSe_2$ after 3 h PEC test in 0.5 M $H_2SO_4$. The peaks of the samples were referenced to those of $MoS_2$ (JCPDS No. 87-2416, $P6_3/mmc$, $a$ = 3.160, $c$ = 12.290 Å), $MoSe_2$ (JCPDS No. 29-0914, $P6_3/mmc$, $a$ = 3.287 Å, $c$ = 12.925 Å), $WS_2$ (JCPDS No. 08-0237, $P6_3/mmc$, $a$ = 3.154 Å, $c$ = 12.362 Å), and $WSe_2$ (JCPDS No. 38-1388, $P6_3/mmc$, $a$ = 3.285 Å, $c$ = 12.982). (b) HAADF STEM image, EDX elemental mapping of Si, O, Mo (or W), and S (or Se) elements, and corresponding EDX spectrum for Si-$MoS_2$, Si-$MoSe_2$, Si-$WS_2$, and Si-$WSe_2$. (c) Survey and fine-scanned XPS data of W 4*f*, S 2*p*, and Si 2*p* peaks of Si-$WS_2$ before/after 3 h PEC test. The data points (open circles) are fitted by Voigt functions. A laboratory-based spectrometer was used with a photon energy of 1486.6 eV (Al Kα). So the peak position and shapes are different from those shown in Fig. S5.

After the PEC, the XRD peaks matched the 2H phase of TMD nanosheets, indicating the phase remains the same as that of as-grown samples. The EDX data shows that the TMD nanosheets remain on the Si NWs and the ratio of M:X is about 1:1.8, which is almost the same as that of before. The EDX mapping of individual NCs before/after the PEC shows that the samples consisted of the Si NW and the TMD shell, and the core-shell structures are persistent during the PEC reaction. The XPS spectrum was examined for Si-$WS_2$ as a representative sample. Fine-scanned XPS data of W 4*f*, S 2*p*, and Si 2*p* peaks of before/after samples show that the peak feature and position remains nearly the same.

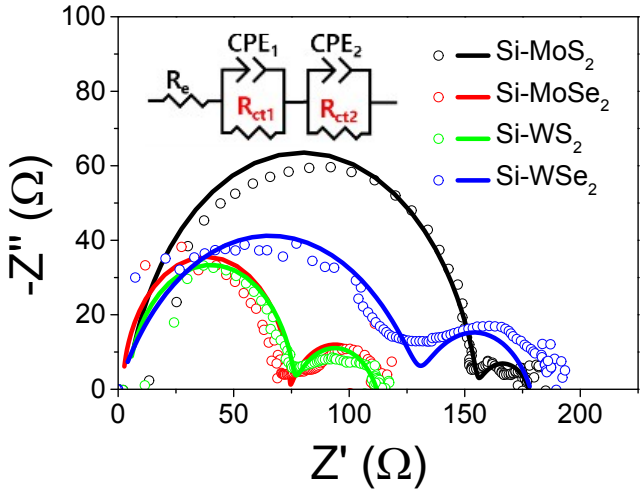


**Fig. S11** Nyquist plots of Si-$MoS_2$, Si-$MoSe_2$, Si-$WS_2$, and Si-$WSe_2$ in 0.5 M $H_2SO_4$ (pH 0) measured for EIS in the frequency range from 1 MHz to 0.1 Hz, under AM1.5G irradiation (100 mW $cm^{-2}$). The applied potential is 0 V (vs. RHE) for HER. The equivalent circuit is shown in the inset of (a), and the fitting curves are represented by the solid lines. The circuit diagram is shown in the inset.

The simulation of EIS spectra (fitted lines) using an equivalent circuit model yielded the $R_{ct}$ values ($R_{ct1}$ and $R_{ct2}$), with the corresponding CPE ($CPE_1$ and $CPE_2$). Under light irradiation, the value of $R_{ct}$ (= $R_{ct1}$ + $R_{ct2}$) is 172, 112, 109, and 203 Ω, respectively, for Si-$MoS_2$, Si-$MoSe_2$, Si-$WS_2$, and Si-$WSe_2$. The similar values indicate the comparable photoinduced charge transfer at the electrode-electrolyte interface. The fitting parameters are summarized as follows.

Fitting parameters of Nyquist plots.

| | $MoS_2$ | $MoSe_2$ | $WS_2$ | $WSe_2$ |
|---|---|---|---|---|
| $R_e$ (Ω) | 4.8 | 1.3 | 3.1 | 1.9 |
| $R_{ct1}$ (Ω) | 149 | 75 | 73 | 161 |
| $R_{ct2}$ (Ω) | 23 | 37 | 36 | 42 |
| $CPE_1$ (F) | $8.7 \times 10^{-9}$ | $1.1 \times 10^{-8}$ | $5.3 \times 10^{-9}$ | $1.6 \times 10^{-4}$ |
| $CPE_2$ (F) | $5.6 \times 10^{-1}$ | $9.7 \times 10^{-4}$ | $1.3 \times 10^{-4}$ | $8.8 \times 10^{-8}$ |
| $R_{ct1} + R_{ct2}$ (Ω) | 172 | 112 | 109 | 203 |

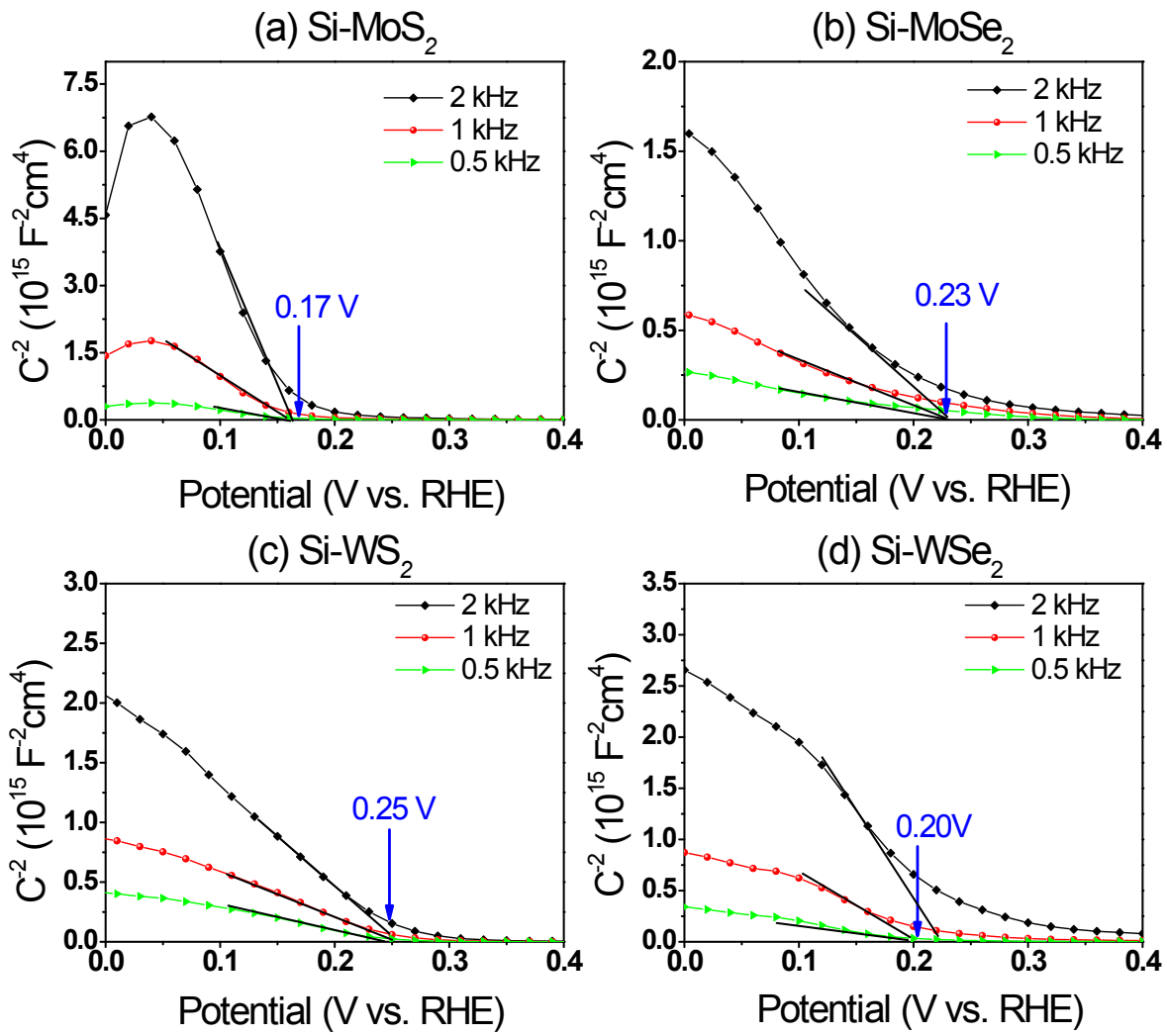


**Fig. S12** Mott-Schottky plots at 0.5, 1, and 2 kHz for (a) Si-$MoS_2$, (b) Si-$MoSe_2$, (c) Si-$WS_2$, and (d) Si-$WSe_2$ in 0.5 M $H_2SO_4$ (pH 0). The flat band potentials ($E_{fb}$) are obtained from the intercepts of the extrapolated lines; 0.17 V for Si-$MoS_2$, 0.23 V Si-$MoSe_2$, 0.25 V for Si-$WS_2$, and 0.20 V Si-$WSe_2$.

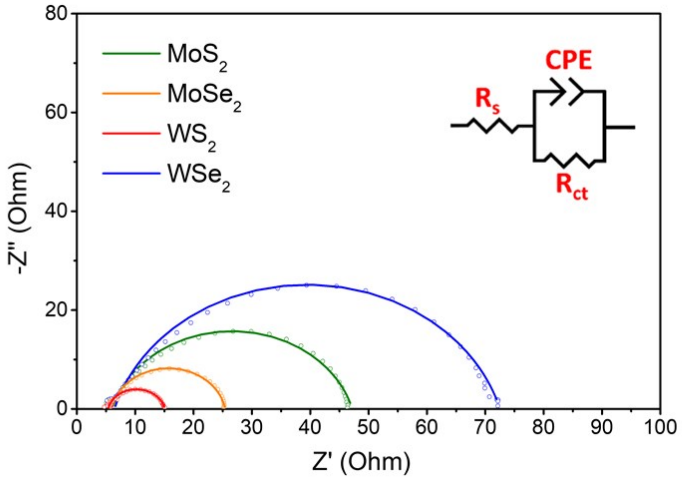


| at 200 mV | $R_s$ (Ω) | $R_{ct}$ (Ω) |
|---|---|---|
| $MoS_2$ | 5.7 | 40.99 |
| $MoSe_2$ | 5.6 | 19.55 |
| $WS_2$ | 5.7 | 9.1 |
| $WSe_2$ | 5.8 | 66.39 |

**Fig. S13** Nyquist plots for EIS measurements of $MoS_2$, $MoSe_2$, $WS_2$, and $WSe_2$ nanosheets, using the frequency in the range from 100 kHz to 0.1 Hz at a representative potential of -0.2 V (vs. RHE). The plots in the right panel corresponds to the magnified one in the marked area on the left plot. The modified Randles circuit for fitting is shown. The data points and the fitting curves are represented by the circles and black line, respectively.

Electrochemical impedance spectroscopy (EIS) measurements of the samples were performed using a 100 kHz–0.1 Hz frequency range and an amplitude of 10 mV at $\eta = 0.2$ V. In the high-frequency limit and under non-Faradaic conditions, the electrochemical system is approximated by the modified Randles circuit shown in the inset, where $R_s$ denotes the solution resistance, CPE is a constant-phase element related to the double-layer capacitance, and $R_{ct}$ is the charge-transfer resistance from any residual Faradaic processes. A semicircle in the low-frequency region of the Nyquist plots represents the charge transfer process, with the diameter of the semicircle reflecting the charge-transfer resistance. The real ($Z'$) and negative imaginary ($-Z''$) components of the impedance are plotted on the $x$ and $y$ axes, respectively. The simulation of the EIS spectra using an equivalent circuit model allowed us to determine the charge transfer resistance, $R_{ct}$, which is a key parameter for characterizing the catalyst-electrolyte charge transfer process. The fitting parameters of $R_s$ and $R_{ct}$ (in Ω) are listed above.

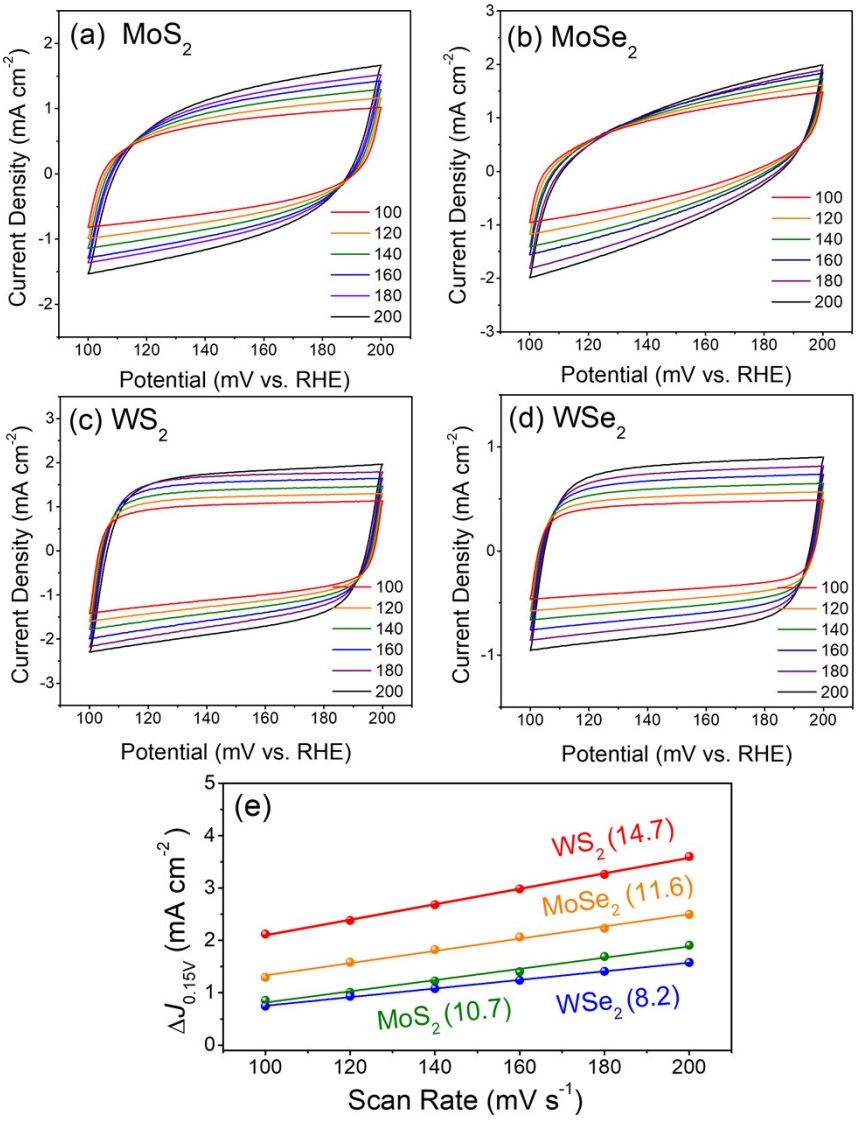


**Fig. S14** Cyclic voltammetry (CV) curves of $MoS_2$, $MoSe_2$, $WS_2$, and $WSe_2$ nanosheets in a non-Faradaic region (0.1-0.2 V vs. RHE), at 100-200 mV $s^{-1}$ scan rates (with a step of 20 mV $s^{-1}$) and in 0.5 M $H_2SO_4$ solution. Difference ($\Delta J$) between the anodic charging and cathodic discharging currents measured at 0.15 V (vs. RHE) and plotted as a function of the scan rate. The value in parenthesis represents the double-layer capacitance ($C_{dl}$), obtained by the half of the linear slope. CV data were measured at 0.1-0.2 V, in a non-Faradaic region. The $C_{dl}$ was obtained as the slope (half value) of a linear fit of $\Delta J$ *vs.* scan rate (100-200 mV $s^{-1}$), where $\Delta J$ is the difference between the anodic charging (positive value) and cathodic discharging currents (positive value). The $C_{dl}$ value in a unit of mF $cm^{-2}$. The $C_{dl}$ value is 10.7, 11.6, 14.7, and 8.2 mF $cm^{-2}$, respectively, for $MoS_2$, $MoSe_2$, $WS_2$, and $WSe_2$. The sample with higher catalytic activity consistently exhibits a larger charge capacitance. Therefore, the double-layer capacitance determines the HER catalytic activity of samples.

**References**


S1. D. Merki, S. Fierro, H. Vrubel and X. Hu, *Chem. Sci.*, 2011, **2**, 1262-1267.

S2. M. A. R. Anjum, H. Y. Jeong, M. H. Lee, H. S. Shin and J. S. Lee, *Adv. Mater.*, 2018, **30**, 1707105.

S3. Y. Hou, B. L. Abrams, P. C. K. Vesborg, M. E. Björketun, K. Herbst, L. Bech, A. M. Setti, C. D. Damsgaard, T. Pedersen, O. Hansen, J. Rossmeisl, S. Dahl, J. K. Nørskov and I. Chorkendorff, *Nat. Mater.*, 2011, **10**, 434-438.

S4. P. D. Tran, S. S. Pramana, V. S. Kale, M. Nguyen, S. Y. Chiam, S. K. Batabyal, L. H. Wong, J. Barber and J. Loo, *Chem. Eur. J.*, 2012, **18**, 13994-13999.

S5. Q. Ding, F. Meng, C. R. English, M. C. Acevedo, M. J. Shearer, D. Liang, A. S. Daniel, R. J. Hamers and S. Jin, *J. Am. Chem. Soc.*, 2014, **136**, 8504−8507.

S6. Q. Ding, J. Zhai, M. Cabán-Acevedo, M. J. Shearer, L. Li, H. -C. Chang, M. -L. Tsai, D. Ma, X. Zhang, R. J. Hamers, J. -H. He and S. Jin, *Adv. Mater.*, 2015, **27**, 6511-6518.

S7. L. Zhang, C. Liu, A. B. Wong, J. Resasco and P. Yang, *Nano Res.*, 2015, **8**, 281-287.

S8. K. C. Kwon, S. Choi, K. Hong, C. W. Moon, Y. -S. Shim, D. H. Kim, T. Kim, W. Sohn, J. -M. Jeon, C. -H. Lee, K. T. Nam, S. Han, S. Y. Kim and H. W. Jang, *Energy Environ. Sci.*, 2016, **9**, 2240-2248.

S9. C. -J. Chen, K. -C. Yang, C. -W. Liu, Y. -R. Lu, C. -L. Dong, D. -H. Wei, S. -F. Hu and R. -S. Liu, *Nano Energy*, 2017, **32**, 422-432.

S10. Y. Hou, Z. Zhu, Y. Xu, F. Guo, J. Zhang and X. Wang*, J. Hydrogen Energy*, 2017, **42**, 2832-2838.

S11. S. Oh, J. B. Kim, J. T. Song, J. Oh and S. -H. Kim, *J. Mater. Chem. A*, 2017, **5**, 3304–3310.

S12. R. Fan, J. Mao, Z. Yin, J. Jie, W. Dong, L. Fang, F. Zheng and M. Shen, *ACS Appl. Mater. Interfaces*, 2017, **9**, 6123−6129.

S13. L. A. King, T. R. Hellstern, J. Park, R. Sinclair and T. F. Jaramillo, *ACS Appl. Mater. Interfaces*, 2017, **9**, 36792-36798.

S14. J. Joe, C. Bae, E. Kim, T. A. Ho, H. Yang, J. H. Park and H. Shin, *Catalysts*, 2018, **8**, 580.

S15. G. Huang, J. Mao, R. Fan, Z. Yin, X. Wu, J. Jie, Z. Kang and M. Shen, *Appl. Phys. Lett.*, 2018, **112**, 013902.

S16. D. M. Andoshe, G. Jin, C. -S. Lee, C. Kim, K. C. Kwon, S. Choi, W. Sohn, C. W. Moon, S. H. Lee, J. M. Suh, S. Kang, J. Park, H. Heo, J. K. Kim, S. Han, M. H. Jo and H. W. Jang, *Adv. Sustainable Syst.*, 2018, **2**, 1700142.

S17. Q. Zhou, S. Su, D. Hu, L. Lin, Z. Yan, X. Gao, Z. Zhang and J. -M. Liu, *Nanotechnology*, 2018, **29**, 105402.

S18. R. Fan, G. Huang, Y. Wang, Z. Mi and M. Shen, *Appl. Catal. B*, 2018, **237**, 158-165.

S19. M. Alqahtani, S. Sathasivam, F. Cui, L. Steier, X. Xia, C. Blackman, E. Kim, H. Shin, M. Benamara, Y. I. Mazur, G. J. Salamo, I. P. Parkin, H. Liua and J. Wu, *J. Mater. Chem. A*, 2019, **7**, 8550–8558.

S20. S. Seo, S. Kim, H. Choi, J. Lee, H. Yoon, G. Piao, J. C. Park, Y. Jung, J. Song, S. Y. Jeong, H. Park and S. Lee, *Adv. Sci.*, 2019, **6**, 1900301.

S21. A. Hasani, Q. V. Le, M. Tekalgne, M. -J. Choi, T. H. Lee, S. H. Ahn, H. W. Jang and S. Y. Kim, *ACS Appl. Mater. Interfaces*, 2019, **11**, 29910-29916.

S22. R. Fan, J. Zhou, W. Xun, S. Cheng, S. Vanka, T. Cai, S. Ju, Z. Mi and M. Shen, *Nano Energy*, 2020, **71**, 104631.